Possible threshold controls on sediment grain properties of Peruvian coastal river basins

Camille Litty[1], Fritz Schlunegger[1], Willem Viveen[2]

[1] *Institute of Geological Sciences, University of Bern, Baltzerstrasse 1+3, CH- 3012 Bern.*

[2] *Area de Geología, Sección de Ingeniería de Minas, Departamento de Ingeniería, Pontificia Universidad Católica del Perú, Av. Universitaria 1801, San Miguel, Lima, Perú.*

ABSTRACT

Twenty-one coastal rivers located along the entire western Peruvian margin were analyzed to determine possible controls on sediment grain properties. This represents one of the largest grain size dataset that has been collected over a large area. Modern gravel beds were sampled along a north-south transect on the western side of the Peruvian Andes where the rivers cross the tip of the mountain range, and at each site the long *a*-axis and the intermediate *b*-axis of about 500 pebbles were measured. Morphometric properties of each drainage basin, sediment and water discharge together with flow shear stresses were determined and compared against measured grain properties. Grain size data show that the values for the D_{50} are nearly constant and range between 2-3 cm, while the values of the D_{96} range between 6 and 12 cm. The ratios between the intermediate and the long axis range from 0.67 to 0.74. Linear correlations between all grain size percentiles and water shear stresses, mean basin denudation rates, mean basin slopes and basin sizes are small to non-existent. However exceptionally large D_{50} values of 4-6 cm were measured for basins situated between 11-12°S and 16-17°S latitude where hillslope gradients are steeper

than on the average or where mean annual stream flows exceed the average values of the western Peruvian streams by a factor of 2. We suggest that the generally uniform grain size pattern has been perturbed where either mean basin slopes, or water fluxes exceed threshold conditions.

1. INTRODUCTION

The size and shape of gravels bear crucial information about (i) the transport dynamics of mountain rivers (Hjulström, 1935; Shields, 1936; Blissenbach, 1952; Koiter et al., 2013; Whittaker et al., 2007; Duller et al., 2012; Attal et al., 2015), (ii) the mechanisms of sediment supply and provenance (Parker, 1991; Paola et al., 1992a, b; Attal and Lavé, 2006), and (iii) environmental conditions such as uplift and precipitation (Heller and Paola, 1992; Robinson and Slingerland, 1998; Foreman et al., 2012; Allen et al., 2013; Foreman, 2014). The mechanisms by which grain size and shape change from source to sink have often been studied with flume experiments (e.g. McLaren and Bowles, 1985; Lisle et al., 1993) and numerical models (Hoey and Ferguson, 1994). These studies have mainly been directed towards exploring the controls on the downstream reduction in grain size of gravel beds (Schumm and Stevens, 1973; Hoey and Fergusson, 1994; Surian, 2002; Fedele and Paola, 2007; Allen et al., 2016). In addition, it has been proposed that the grain size distribution particularly of mountainous rivers mainly depends on: (i) tectonic uplift resulting in steepening of the entire landscape (Dadson et al., 2003; Wittmann et al., 2007; Ouimet et al., 2009), (ii) earthquakes and seismicity causing the release of large volumes of landslides (Dadson et al., 2003; McPhillips et al., 2014); (iii) precipitation rates and patterns controlling river discharge and shear stresses (D'Arcy et al., 2017; Litty et al., 2017); and (iv) bedrock lithology where low erodibilty lithologies are sources of larger volumes of material (Korup and Schlunegger, 2009, Allen et al., 2015). Accordingly, the sediment caliber

in these rivers could either reflect the nature of erosional processes in the headwaters and conditions thereof (such as lithology, slope angles, seismicity releasing landslides), which then corresponds to supply-limited conditions. Alternatively, if enough material is supplied to the streams, then the grain size pattern mainly depends on the runoff and related shear stresses in these rivers, which in turn corresponds to transport-limited conditions.

The western margin of the Peruvian Andes represents a prime example where these mechanisms and related controls on the grain size distribution of river sediments can be explored. In particular, this mountain belt experiences intense and frequent earthquakes (Nocquet et al., 2014) in response to subduction of the oceanic Nazca plate beneath the continental South American plate at least since late Jurassic times (Isacks, 1988). Therefore, it is not surprising that erosion and the transfer of material from the hillslopes to the rivers has been considered to strongly depend on the occurrence of earthquakes (McPhilipps et al., 2014). On the other hand, it has also been proposed that denudation in this part of the Andes is controlled by distinct precipitation rate gradients. These inferences have been made based on concentrations of in-situ cosmogenic ^{10}Be measured in river-born quartz (Abbühl et al., 2011; Carretier et al., 2015; Reber et al., 2017), and on morphometric analyses of the western Andean landscape (Montgomery et al., 2001). Accordingly, erosion along the western Peruvian Andes has been related to either the occurrence of earthquakes and thus to tectonic processes (McPhillips et al., 2014) or rainfall rates (Abbühl et al., 2011; Carretier et al., 2015) and thus to the stream's mean annual runoff (Reber et al., 2017). Therefore, we hypothesize that hillslope erosion paired with the streams runoff are likely to have a measurable impact on the grain size pattern in the Peruvian streams.

Here we present data on sediment grain properties from rivers situated on the western margin of the Peruvian Andes (Figure 1A) in order to elucidate the possible effects of intrinsic factors such

as morphometric properties of the drainage basins (mean slope, drainage area, stream lengths), and extrinsic properties (runoff and seismic activity) on sediment grain properties. To this extent, we collected grain size data from gravel bars of each stream along the entire western Andean margin of Peru that are derived from 21, over 700-km^2-large basins. Sampling sites were situated at the outlets of valleys close to the Pacific Coast. This represents one of the largest grain size datasets that have ever been collected over areas which have experienced different tectonic and climatic conditions.

1.1 Geologic and tectonic setting

The study area is located at the transition from the Peruvian Andes to the coastal lowlands along a transect from the cities of Trujillo in the north (8°S) to Tacna in the south (18°S). In northern and central Peru, a flat, up-to 100 km wide, broad coastal forearc plain with Paleogene-Neogene and Quaternary sediments connects to the western Cordillera. This part of the western Cordillera consists of Cretaceous to late Miocene plutons of various compositions (diorite, but also tonalite, granite and granodiorite) that crop out over an almost continuous, 1600-km long arc that is referred to as the Coastal Batholith (e.g. Atherton, 1984; Mukasa, 1986; Haederle and Atherton, 2002; Figure 1B). In southern Peru, the coastal plain gives way to the Coastal Cordillera that extends far into Chile. The western Cordillera comprises the central volcanic arc region of the Peruvian Andes with altitudes of up to 6768 m.a.s.l., where currently active volcanoes south of 14°S of latitude are related to a steep slab subduction. On the other hand, Cenozoic volcanoes in the central and northern Peruvian arc have been extinct since c. 11 Ma due to a flat slab subduction, which inhibited magma upwelling from the asthenosphere (Ramos, 2010).

The bedrock of the Western Cordillera is dominated by Paleogene, Neogene and Quaternary volcanic rocks (mainly andesitic or dacitic tuffs, and ignimbrites) originating from distinct phases of Cenozoic volcanic activity (Vidal, 1993). These rocks rest on Mesozoic and Early Paleogene sedimentary rocks (Figure 1B).

The tectonic conditions of the western Andes are characterized by strong N-S gradients in Quaternary uplift, seismicity and long-term subduction processes, which in turn seem controlled by a plethora of tectonic processes. The northern segment of the coastal Peruvian margin (i.e. to the north of 13°S latitude), hosts a coastal plain that shows little evidence for uplift, and the Nazca plate subducts at a low angle. Also in this region, the occurrence of large historical earthquakes at least along the coastal segment has been much less (Figure 2c). Only in northernmost Peru (4° to 6° S latitude) uplift of the coastal area is associated with subduction earthquakes (Bourgois et al., 2007). Further south, in the Cordillera Blanca area (around 12° S latitude) may have been uplifted due to upwelling of magma (McNulty and Farber, 2002). In particular, the coastal segment south of 13°S hosts raised Quaternary marine terraces (Regard et al., 2010), suggesting the occurrence of surface uplift at least during Quaternary times. Since the number and altitude of the terraces increases closer to the area where currently the Nazca ridge subducts, uplift of the coastal area in a radius of approximately 200 km around the ridge (roughly 12° to 14° S latitude) is attributed to ridge subduction (Sébrier et al., 1988; Macharé and Ortlieb, 1992). Between 15° and 18° S latitude, uplift is associated with bending of the Bolivian orocline (Noury et al., 2016). The area south of 12° S latitude is also the segment of the Andes where the number of earthquakes with magnitudes > 4 has been large relative to the segment farther north (Figures 1 and 2c). In contrast, the northern segment of the coastal Peruvian margin (i.e., to the north of 13°S latitude), hosts a coastal plain that has been subsiding and the Nazca plate subducts

115 at a low angle. Also in this region, the frequency of large historical earthquakes at least along the
116 coastal segment has been much less (Figure 2c)
117
118 ***1.2 Morphology***
119 The local relief along the western Cordillera has been formed by deeply incising rivers that flow
120 perpendicular to the strike of the Andes (Schildgen et al., 2007). The morphology of the
121 longitudinal stream profiles is characterized by two segments separated by a distinct knickzone
122 (Trauerstein et al., 2013). These geomorphic features have formed through headward retreat in
123 response to a phase of enhanced surface uplift during the late Miocene (e.g., Schildgen et al.,
124 2007). Upstream of these knickzones, the streams are mainly underlain by Cenozoic
125 volcanoclastic rocks, while farther downstream incision has disclosed the Coastal Batholith and
126 older meta-sedimentary units (Trauerstein et al. 2013). The upstream edges of these knickzones
127 also delineate the upper boundaries of the major sediment sources (Litty et al., 2017). Little to
128 nearly zero clastic material has been derived from the headwater reaches on the Altiplano, where
129 the flat landscape has experienced nearly zero erosion, as 10Be-based denudation rate estimates
130 (Abbühl et al., 2011) and provenance tracing have shown (Litty et al., 2017).
131 The pattern of mean slopes per drainage basin reveals a distinct N-S trend (Table 1). The
132 corresponding values increase from 20° to 25° going from 6°S to 10°S latitude (where they reach
133 maximum values between 0.4 to 0.45 m/m) after which they decrease by nearly 50% to values
134 ranging between 10° and 15°. These relationships have not been explored yet, but most likely
135 reflect the extent to which streams have crossed the western escarpment and sourced their waters
136 in the relatively flat plateau of the Puna region. Indeed, most of the western Peruvian streams
137 have their water sources on this flat area and then cross the western escarpment, which yields

relatively low mean basin slopes particularly for basins south of 12°S. Contrariwise, the basins around 11°-12°S latitudes (which are characterized by the steep slopes) have their sources in the relatively steep Cordillera Negra (Figure 1A), which is a relatively dry mountain range situated on the steep escarpment. Along these latitudes, the high Andes are constituted by the high and heavily glaciated Cordillera Blanca situated farther to the east (Figure 1A). This mountain range is drained by the Rio Santa, which flows parallel to the Andes strike within the valley of the Rio Santa , and then crosses the Cordillera Negra at a right angle (Figure 1A).

1.2 Climatic setting and runoff of streams

The Peruvian western margin shows an E-W contrasting precipitation pattern with high annual precipitation rates up to 800 mm on the Altiplano and c. 0 mm per year on the coast ((Huffman et al., 2007; Figure 1C). This precipitation gradient in the western Andes is related to the position of the Intertropical Convergence Zone (ITCZ, inset of Figure 1C) associated with an orographic effect on the eastern side of the Andes (Bookhagen and Strecker, 2008). During austral summer (January) the center of the ITCZ is located farther south, transferring the moisture from the Amazon tropical basin to the Altiplano (Garreaud et al., 2009) and leading to a wet climate on the Altiplano with high precipitation rates. During austral winter, the Altiplano is under the influence of dry air masses from the subsiding branch of the Hadley cell that result in a more equatorial position of the ITCZ and in a dry persistent westerly wind with almost no precipitation on the Altiplano. Additionally, the Andes form an orogenic barrier preventing Atlantic winds and moisture from reaching the coast. In addition, every 2 to 10 years, near to the Equator, the Pacific coast is subjected to strong precipitation resulting in high flood variability, related to the El Niño weather phenomenon (DeVries, 1987).

Mean annual discharge of streams along the western Peruvian margin has been reported by Reber et al. (2017). These authors calculated mean annual discharge values using the TRMM-V6.3B43.2 precipitation database by Huffman et al. (2007) as a basis. Reber et al. (2017, see their Table 3) corrected the theoretical values for water losses due to evaporation and irrigation using the gauging record of a minimum of 12 basins situated close to the Pacific ocean. For these areas hydrological data has been reported by the Sistema Nacional de Información de Recursos Hídricos (SNIRH). The hydrological data thus cover a time span of c. 12 years. The results show a pattern where mean annual ruonff of these streams ranges between c. 10-40 m^3/s. Rivers where mean annual runoff values are nearly 80 m^3/s comprise the Rio Santa at c. 9°S latitude (Figure 1A), which derives its water from glaciers in the Cordillera Blanca. Two other streams with high discharge values are situated at 16°-17°S (Rio Ocoña and Rio Camaña, Figure 1A) where the corresponding headwaters spread over a relatively large area across the Altiplano, thereby collecting more rain than the other basins.

2. SITE SELECTION AND METHODS

Sampling sites are situated in the main river valleys in the western Cordillera between 8°S and 18°S latitude just before it gives way to the coastal margin. Only the 21 main river basins were selected, which were generally larger than 700 km^2. We selected the downstream end of these rivers for simplicity because this yields comparable conditions as the base level is the same for all streams. Sampling sites are all accessible along the Pan-American Highway (see Table 1 for the coordinates of the sampling sites). Additionally, the Majes basin (marked with red color on Figure 1A) has been sampled at five sites from upstream to downstream to explore the effects related to the sediment transport processes for a section across the mountain belt, but along the

stream (Figure 3; Table 2). The Majes basin has been chosen because of its easy accessibility in the upstream direction and because the morphology of this basin has been analyzed in a previous study (Steffen et al., 2010).

We randomly selected five longitudinal bars where we collected our grain size dataset. It has been shown that using a standard frame with fixed dimensions to assist gravel sampling reduces user-biased selections of gravels (Marcus et al., 1995; Bunte and Abt, 2001a). In order to reduce this bias, we substituted the frame by shooting an equal number of photos at a fixed distance (c. 1 m) from the ground surface at each longitudinal bar. Ten photos were taken from an approximately 10 m^2-large area to take potential spatial variabilities among the gravel bars into account. From those photos, the intermediate *b*-axes and the ratio of the *b*-axes and the long *a*-axis of around 500 randomly chosen pebbles were manually measured (Bunte and Abt, 2001b) and processed using the software program ImageJ (Rasband, 1997). Our sample population exceeds the minimum number of samples needed for statistically reliable estimations of grain size distributions in gravel bars (Howard, 1993; Rice and Church, 1998).

The pebbles were characterized on the basis of their median (D_{50}), the D_{84} and the coarse (D_{96}) fractions. This means that 50%, 84% and 96% of the sampled fraction is finer grained than the 50^{th}, 84^{th} and 96^{th} percentiles of the samples. On a gravel bar, pebbles tend to lie with their short axis perpendicular to the surface, thus exposing their section that contains the *a*- and *b*-axes (Bunte and Abt, 2001b). However, the principal limitation is the inability to accurately measure the fine particles < 3 mm (see also Whittaker et al., 2010). While we cannot resolve this problem with the techniques available, we do not expect that this adds a substantial bias in the grain size distributions reported here as their relative contributions to the point count results are minor (i.e. < 5%, based on visual inspection of the digital images).

Catchment-scale morphometric parameters and characteristics, including drainage area, mean slope angle for each catchment, slope angle of the stream channel at the sampling site and distances from the sample sites to the upper edge of the Western Escarpment were extracted from the 90-m-resolution digital elevation model (DEM) Shuttle Radar Topography Mission (SRTM; Reuter et al., 2007).

Because grain size patterns largely depend on water shear stresses, we explored where such correlations might exist. We thus computed water shear stresses τ following Hancock and Anderson (2002) and Litty et al. (2016), where:

$$\tau = 0.54pg\left(\frac{Q}{W}\right)^{0.55} S^{0.93} \quad (1).$$

Here, ρ=*1000 kg/m*^{3} is the water density, g the gravitational acceleration, Q (*m*^{3}*/s*) is mean annual water discharge that we have taken from Reber et al. (2017), W (*m*) the channel width, and S (*m/m*) is the channel gradient. Stream channel widths with an estimated error of 2 m were measured on satellite images where available, and on photos taken during the field campaign.

We were also interested in exploring whether sediment flux has a measurable impact on the grain size pattern because higher denudation rates could be associated with the supply of more coarse-grained material to the trunk stream This in turn could result in larger clasts in these streams and this could potentially cause gravel fronts to shift towards more distal sites (Dingle et al., 2017), thereby coarsening the sediment caliber at our sampling sites.These basins have recently been analyzed for ^{10}Be-based catchment averaged denudation rates and mean annual water fluxes (please see Reber et al., 2017, and information presented above). This allows us to explore whether sediment flux, which equals the product between ^{10}Be-based denudation rates and basin size, has a measurable impact on the grain size pattern. We have considered the ^{10}Be-based

basin mean denudation rates (Reber et al., 2017; Table 1) as variable because higher denudation rates could be associated with the supply of more coarse-grained material to the trunk stream, which in turn could result in larger clasts in these streams. Furthermore, we also calculated mean basin sediment fluxes as a product between ^{10}Be-based denudation rates and basin size. We considered this variable because

Possible covariations and correlations between grain size and/or morphometric parameters and basin characteristics were evaluated using Pearson correlation coefficients, thus providing corresponding r-values (Table 3). The r-values measure the linear correlations between variables. The values range between +1 and −1, where +1 reflects a 100% positive linear correlation, 0 reflects no linear correlation, and −1 indicates a 100% negative linear correlation (Pearson, 1895). Threshold values of > + 0.30 and < - 0.30 were selected to assign positive and negative correlations, respectively.

3. RESULTS

3.1 Grain size

The results of the grain size measurements reveal a large variation for the *b*-axis where the values of the D_{50} range from 1.3 cm to 5.5 cm (Figure 2h; Table 1). Likewise, D_{84} values vary between 3 cm and 10.5 cm. The sizes for the D_{96} reveal the largest spread, ranging from 6 cm to 31 cm. The ratio between the lengths of the *b*-axis and *a*-axis (sphericity ratio) is nearly constant and varies between 0.67 and 0.74 (Figure 2i). Note that between 15.6°S and 13.7°S, no gravel bars are encountered in the rivers where they leave the mountain range, and only sand bars can be found. Therefore no results are exhibited for these latitudes (Figure 2h and 2i).

3.2 The Majes basin

The D_{50} percentile of the *b*-axis decreases from 6.2 cm to a value of 5.2 cm c. 80 km farther downstream (Figures 3 and 4 and Table 2). Likewise, the D_{84} decreases from 19 cm to 8.7 cm, and the D_{96} decreases from 31 cm to 11.6 cm (Figure 4). Geomorphologists widely accept the notion that the downstream hydraulic geometry of alluvial channels reflects the decrease of particle size within an equilibrated system involving stream flow, channel gradient, sediment supply and transport (Hoey and Ferguson, 1994; Fedele and Paola, 2007; Attal and Lavé, 2009). Sternberg (1875) formalized these relations and predicted an exponential decline in particle size in gravel-bed rivers as a consequence of abrasion and selective transport where the gravel is transported downstream. The relation follows the form: $D_x = D_0\ e^{-\alpha x}$ (Sternberg, 1875). Here, the exponent α decreases from 0.3 for the D_{96} to 0.1 for the D_{50} (Figure 4).

3.3 Correlations between grain sizes and morphometric properties

Table 3 shows the Pearson correlation coefficients (r-value) between the grain sizes, the morphometric parameters and the characteristics of the basins. As was expected, the D_{50}, D_{84} and D_{96} all strongly correlate with each other ($0.73 < \text{r-value} < 0.93$), but the *b/a* ratios do not correlate with any of the three percentiles ($-0.1 < \text{r-value} < 0.1$). Likewise, inter-correlation relationships also exist among other variables such as catchment area, distance from the western escarpment, sediment flux and water discharge (Table 3). The D_{50} values positively but weakly correlate with the sizes of the catchment area (r-value = 0.31), the distances from the Western Escarpment (r-value = 0.35), the mean annual shear stress at the sampling site (r-value = 0.23), the denudation rates (r-value = 0.34) and the sediment fluxes (r-value = 0.42; Table 3). The D_{84} and the D_{96} values correlate positively with the mean annual shear stress exerted by the water

flux with a r-value of 0.33 and 0.39 (Table 3). However, we note that these correlations are weak, and some might break apart if the largest values for e.g. shear stresses (Table 3) are removed.

At a broader scale, values of the D_{50} are nearly constant between 2 and 3 cm (Table 3). The largest D_{50} with values of up to 6 cm are encountered in streams that are either sourced in the Cordillera Negra where mean basin slope angles are larger than 20°, or in the Rio Ocoña and Rio Camaña rivers located at 16°-17°S, which have the largest mean annual discharge as they capture their waters from a broad area on the Altiplano.

The ratio of the intermediate axis over the long axis negatively correlates with the distance from the Western Escarpment (r-value = -0.33), albeit with a poor correlation, but a strong and positive correlation is found with the mean slope angles of the basins (r-value = 0.63; Table 3).

4. DISCUSSION

4.1 SLOPE ANGLE CONTROLS ON SPHERICITY

The poor negative correlation of -0.33 between the sphericity of the pebbles and distance from the escarpment edge (Table 3) prevents us from inferring a distinct control of this variable. On the other hand, the positive Pearson correlation of 0.63 between the sphericity of the pebbles and the mean basin slope is quite high (Table 3), thus pointing towards a significant control. This suggests that basins with steeper slopes produce rounder pebbles. We do not consider that this pattern is due to differences in exposed bedrock in the hinterland because the litho-tectonic architecture is fairly constant along the entire Peruvian margin (Figure 1). We tentatively infer that time scales of transport and evacuation of material are likely to be shorter in steeper basins

298 compared to shallower ones. This might influence the shape of pebbles as they tend to flatten as
299 effects of abrasion and 3D heterogeneities of bedrock that becomes more obvious with time and
300 transport distance (Sneed and Folk, 1958). We thus see the positive correlation between mean
301 hillslope angle and the sphericity of pebbles as a very likely consequence of shorter transport
302 times in steeper basins, but we note that this hypothesis needs to be confirmed by detailed real-
303 time surveys of material transport from sources down to the end of these rivers.
304
305 4.2 CONTROLS ON GRAIN SIZE
306 *Downstream fining trends in the Majes basin indicate fluvial controls*
307 In fluvial environments, the sorting of the sediment depends on the downstream distance from its
308 source (Hoey and Ferguson, 1994; Kodoma, 1994; Paola and Seal, 1995). This is particularly the
309 case for the Majes river, where we see an exponential, downstream fining trend (Figure 4). This
310 is somewhat surprising because sufficiently voluminous sediment input from other sources may
311 perturb any downstream fining trends in the grain size distribution (Rice and Church, 1998).
312 Likewise, in the Majes basin, the sediment supply from the hillslopes to the trunk stream has
313 occurred mainly through debris flow processes and landsliding (Steffen et al., 2010; Margirier et
314 al., 2015). So, while the supply of hillslope-dervied material is likely to have been accomplished
315 by mass wasting processes, the evacuation and transport of this sediment down to the Pacific
316 Ocean has occurred mainly through fluvial transport.
317
318 *Grain size and earthquake impact*
319 Landslides and debris flows represent the main processes of hillslope erosion and the main
320 source of sediment in tectonically active orogens (Hovius et al., 1997; Korup et al., 2011). They

321 are generally associated with triggers such as earthquakes or intense rainfall and generally supply
322 coarse and voluminous sediments to the trunk rivers (Dadson et al., 2003; McPhillips et al.,
323 2014). In that sense, we would expect a positive correlation between the frequency of large
324 earthquakes and the grain size where an increase in earthquake frequency would induce an
325 increase in landslide occurrence, thereby supplying coarser grained sediment from the hillslopes
326 to the rivers. These relationships have been elaborated in multiples studies where positive
327 relationships between landslide occurrence and the size of earthquakes have been documented
328 (e.g., Keefer, 1984; 1994; Parker et al., 2011). We note here that a global-scale correlation
329 between earthquake magnitudes and areas affected by landslides suggests that mass movements
330 are triggered by earthquakes if a threshold magnitude of 5.5 is exceeded (Keefer, 1984). Here,
331 we consider earthquakes with magnitudes >4.5 because Figure 1 by Keefer (1984) suggests that
332 earthquakes with magnitudes as low as 4.5 are theoretically able to release landslides over an
333 area larger than 10 km^2, which is already a large area. However, we do not see correlation
334 between the number of recorded historical earthquakes larger than 4.5 Mw and the grain size
335 data (Figure 2c). We then expect that the frequency of earthquakes larger than 4.5 Mw, and
336 related to this, the subduction mechanisms, do not exert a measurable control on the grain size in
337 the rivers of the western Peruvian Andes.
338
339 *Possible threshold limits as controls on the grain size pattern*
340 We consider the correlations between the grain size data and the basins scale properties (basin
341 area, mean basin denudation rates, water shear stresses, sediment fluxes) as weak and
342 unconvincing (Table 3). However, we recall that the D_{50} records a nearly uniform pattern with
343 values that range between 2-3 cm along the studied western Peruvian margin. However, higher

values of up to 6 cm are either measured in streams where mean slope angles of the bordering hillslopes in the upstream basin exceed 20° (between 11° and 12°S) or where water runoff values are nearly twice as large as the mean of all Peruvian streams (ranging between 10-40 m^3/s between 16° and 17°S; see Figure 3 and Table 3). Based on these observations, we tentatively interpret a supply control on the median grain size for the Cordillera Negra streams where slopes are mediating grain size through a threshold effect. In this case, these thresholds on the hillslopes are likely to be conditioned by the at-yield mechanical states of bedrock (Montgomery, 2001; Ouimet et al., 2009), where hillslopes with dip angles up to 20-25° can be sustained. Under these conditions, mass failure processes are likely to dominate the supply of material to the trunk stream, thereby increasing the caliber of the supplied material and causing the bedload material to coarsen. In the same sense, a threshold response to steeper slopes has been interpreted for the pattern of ^{10}Be-based denudation rates in the Andes (Reber et al., 2017) and in the Himalayas (Ouimet et al., 2009). In both cases, the relationships between denudation rates and mean basin slopes was considered to follow a non-linear diffusive mass transport model where denudation rates are proportional to mean basin slopes for low gradients, while these relationships become non-linear for slopes approaching a critical value. Reber et al. (2017) set this critical value to 27.5°, but the linear relationship of their dataset breaks apart for gradients larger than 0.4, which corresponds to an angle of c. 21°. At these conditions, hillslopes approach a threshold where slope angles are limited by the mechanical strength of bedrock (Montgomery, 2001; Schlunegger et al., 2013). Hillslope erosion is then mainly accomplished through mass failure processes, which in turn, is likely to supply more coarse-grained material to the trunk stream (see above), as modern examples have shown (Bekaddour et al., 2013). We note, however, that a confirmation of this hypothesis requires data about the spatial density and frequency of landslide occurrence

367 along the western Peruvian Andes. This dataset, however, is not available yet, and its
368 establishment warrants further investigations.
369 In basins situated between 16°-17°S, mean basin slopes are clearly below threshold conditions,
370 but the D_{50} is twice as large as in neighboring rivers. Interestingly, these streams have mean
371 annual discharge values that are twice as large as the western Peruvian streams on the average.
372 Similar to the Cordillera Negra, we relate the relationships at 16°-17°S to threshold controls. In
373 this case, however, they are likely to be conditioned by transport. The mechanisms by which
374 grain size can be mediated through a threshold effect upon transport are less well understood, but
375 it has been known at least since the engineering work by Shields (1936), and particularly by
376 Peter Meyer Müller (1948) that threshold conditions have to be exceeded and have a control on
377 transport of grains in fluvial streams. As a consequence, at transport-limited conditions, sediment
378 flux, and most likely also the caliber of the transported material, depends on the frequency and
379 the magnitudes at which these thresholds are exceeded rather than on a mean value of water
380 discharge (Dadson et al., 2003). This might be the reason why values of water shear stresses, that
381 are calculated based on the annual mean of water flux, are not sufficiently strongly correlated
382 with the D_{50} values to invoke a strong controls thereof (Table 3). However, the lack of
383 information about discharge patterns prevents us from calculating the magnitude-frequency
384 distribution of runoff. Nevertheless, we consider the occurrence of larger peak floods for streams
385 that capture a large portion of their waters on the Altiplano Plateau. This might indeed be the
386 case for the Rio Ocoña and Rio Camaña. We thus tentatively assign large peak floods for these
387 streams, which might explain the larger D_{50} values encountered in their gravel bars. Although
388 highly speculative, we support our statement by the highly seasonal character of preciptation
389 occurrence particularly on the eastern Andean margin and the Altiplano Plateau, which is largely

390 conditioned by the monsoonal Andean jet (see above). We note, however, that this statement
391 warrants a high resolution hydrological dataset for the western Peruvian sreams, which is not
392 available.
393 An exception from these relationships is presented by the Rio Santa (Figure 1A) where mean
394 annual water discharge reaches a value of almost 80 m^3/s, but where the size of the D_{50} is low.
395 We relate this to the possible supply-limited state of this stream, conditioned by the orogen-
396 parallel valley of the Rio Santa between the Cordillera Blanca and the Cordillera Negra, which
397 has acted as a subsiding graben since the past 5.4 Ma (Giovanni et al., 2010; Margirier et al.,
398 2015) and which might thus have operated as a sediment trap. This interpretation is also
399 consistent with the low ^{10}Be-based catchment averaged denudation rates measured for the Rio
400 Santa basin, as noted by Reber et al. (2017).
401 Note that our inferences are largely based on the pattern of the D_{50}, and that the consideration of
402 the larger percentiles might add alternative views on our interpretations. However, since all
403 percentiles are inter-correlated, as the pattern of the Pearson correlation coefficients suggests
404 (Table 3), we think that our general conclusions about the occurrence of thresholds upon the
405 supply and transport of sediment will not change. Note also that either transport or supply control
406 and related thresholds were identified by Reber et al. (2017) for their explanation of the 10Be-
407 based datasets on basin-averaged denudation rates on the western Peruvian Andes. We
408 tentatively interpret that the grain size pattern of the Peruvian streams follows these lines.
409

410 **Conclusion**

411 We present a complete dataset about grain sizes for all major rivers that are situated on the
412 western Andean margin of Peru. We did not find any correlations to the current seismic regimes,

where a larger occurrence of earthquakes with magnitudes larger than 4.5 Mw is expected to increase the supply of coarse-grained material. However, we found that the values for the D_{50} are nearly constant and range between 2 and 3 cm. Exceptionally larger D_{50} values of 4-6 cm were measured for basins situated between 11-12°S and 16-17°S where hillslope gradients are steeper than average (i.e., 20-22°), and where mean annual stream flows exceed the average values of the western Peruvian streams (10-40 m^3/s) by a factor of 2. We suggest that the generally uniform grain size pattern has been perturbed where either mean basin slopes, or water fluxes exceed threshold conditions upon the supply and the transport of material. This might have implications for our understanding of the controls on the grain size distribution of gravelly-based streams.

ACKNOWLEDGMENTS

This project is funded by the Swiss National Science Foundation (project Number 137516).

REFERENCES CITED

Abbühl, L.M., Norton, K.P., Jansen, J.D., Schlunegger, F., Aldahan, A., and Possnert, G., 2011, Erosion rates and mechanisms of knickzone retreat inferred from 10Be measured across strong climate gradients on the northern and central Andes Western Escarpment: Earth Surface Processes and Landforms, v. 36, p. 1464–1473.

Allen, G. H., Barnes, J. B., Pavelsky, T. M. and Kirby, E., 2013, Lithologic and tectonic controls on bedrock channel form at the northwest Himalayan front: Journal of Geophysical Research: Earth Surface, v. 118, no. 3, p. 1806-1825.

Allen, P.A., Armitage, J.J., Whittaker, A.C., Michael, N.A., Roda-Boluda, D. and D'Arcy, M., 2015, Fragmentation model of the grain size mix of sediment supplied to basins: The Journal of Geology, v. 123, p. 405-427.

438 Allen, P. A., Michael, N. A., D'Arcy, M., Roda-Boluda, D. C., Whittaker, A. C., Duller, R. A.,
439 and Armitage, J. J., 2016. Fractionation of grain size in terrestrial sediment routing
440 systems. Basin Research. v. 29(2), p. 180-202
441 Atherton, M. P., 1984. The coastal batholith of Peru. In Andean Magmatism (pp. 168-179).
442 Birkhäuser Boston.
443 Attal, M. and Lavé, J., 2006, Changes of bedload characteristics along the Marsyandi River
444 (central Nepal): Implications for understanding hillslope sediment supply, sediment load
445 evolution along fluvial networks, and denudation in active orogenic belts: Geological
446 Society of America Special Papers, v. 398, p.143-171.
447 Attal, M. and Lavé, J., 2009. Pebble abrasion during fluvial transport: experimental results and
448 implications for the evolution of the sediment load along rivers. J. Geophys. Res.
449 114:F04023. doi:10.1029/2009JF001328.
450 Attal, M., Mudd, S. M., Hurst, M. D., Weinman, B., Yoo, K. and Naylor, M., 2015, Impact of
451 change in erosion rate and landscape steepness on hillslope and fluvial sediments grain
452 size in the Feather River basin (Sierra Nevada, California): Earth Surface Dynamics, v. 3,
453 p. 201-222.
454 Bekaddour, T., Schlunegger, F., Attal, M. and Norton, K. P., 2013. Lateral sediment sources and
455 knickzones as controls on spatio-temporal variations of sediment transport in an Alpine
456 river. Sedimentology, v. 60(1), p. 342-357.
457 Blissenbach, E., 1952. Relation of surface angle distribution to particle size distribution on
458 alluvial fans: J. Sediment. Petrol., v. 22, p. 25–28.

459 Bookhagen, B. and Strecker, M. R., 2008, Orographic barriers, high-resolution TRMM rainfall,
460 and relief variations along the eastern Andes, Geophysical Research Letters, v. 35, p.
461 L06403.
462 Bourgois, J., Bigot-Cormier, F., Bourles, D., Braucher, R., Dauteuil, O., Witt, C., & Michaud, F.,
463 2007. Tectonic record of strain buildup and abrupt coseismic stress release across the
464 northwestern Peru coastal plain, shelf, and continental slope during the past 200 kyr.
465 Journal of Geophysical Research: Solid Earth, 112(B4).
466 Bunte, K., Abt, S.R., 2001a. Sampling frame for improving pebble count accuracy in coarse
467 gravel-bed rivers. Journal of the American Water Resources Association, v. 37 (4), p.
468 1001- 1014.

469 Bunte, K., Abt, S.R., 2001b. Sampling surface and subsurface particle-size distributions in
470 wadable gravel- and cobble-bed rivers for analyses in sediment transport, hydraulics,
471 and streambed monitoring. General Technical Report RMRS-GTR-74. United States
472 Department of Agriculture; Forest Service; Rocky Mountain Research Station. Fort
473 Collings, USA, p. 428.
474 Carretier, S., Tolorza, V., Rodríguez, M. P., Pepin, E., Aguilar, G., Regard, V. and Hérail, G.,
475 2015. Erosion in the Chilean Andes between 27° S and 39° S: tectonic, climatic and
476 geomorphic control. Geological Society, London, Special Publications, v. 399(1), p. 401-
477 418.
478 Dadson, S. J., Hovius, N., Chen, H., Dade, W. B., Hsieh, M. L., Willett, S. D. and Lague, D.,
479 2003. Links between erosion, runoff variability and seismicity in the Taiwan orogen.
480 Nature, v. 426(6967), p. 648-651.
481 D'arcy, M., Whittaker, A. C., and Roda-Boluda, D. C., 2017. Measuring alluvial fan sensitivity
482 to past climate changes using a self-similarity approach to grain-size fining, Death
483 Valley, California. Sedimentology, v. 64(2), p. 388-424.
484 DeVries, T. J., 1987, A review of geological evidence for ancient El Nino activity in Peru. J.
485 Geophys. Res, v. 92, no. 14, p. 471–14.
486 Dingle, E. H., Attal, M., and Sinclair, H. D., 2017. Abrasion-set limits on Himalayan gravel flux.
487 Nature, v. 544(7651), p. 471-474.
488 Duller, R. A., Whittaker, A. C., Swinehart, J. B., Armitage, J. J., Sinclair, H. D., Bair, A. and
489 Allen, P. A., 2012, Abrupt landscape change post-6 Ma on the central Great Plains,
490 USA: Geology, v. 40, p. 871-874.
491 Fedele, J. J. and Paola C., 2007, Similarity solutions for fluvial sediment fining by selective
492 deposition: Journal of Geophysical Research: Earth Surface (2003–2012), v. 112.
493 Foreman, B. Z., Heller, P. L. and Clementz, M. T., 2012, Fluvial response to abrupt global
494 warming at the Palaeocene/Eocene boundary: Nature, v. 491, no. 7422, p. 92-95
495 Foreman, B. Z., 2014, Climate-driven generation of a fluvial sheet sand body at the Paleocene–
496 Eocene boundary in north-west Wyoming (USA): Basin Research, v. 26, no. 2, p. 225-
497 241.

498 Garreaud, R. D., Vuille, M., Compagnucci, R., and Marengo, J., 2009, Present-day South
499 American climate. Palaeogeography, Palaeoclimatology, Palaeoecology, v. 281, no. 3, p.
500 180-195.
501 Haederle, M. and Atherton, M. P., 2002. Shape and intrusion style of the Coastal Batholith, Peru.
502 Tectonophysics, v. 345(1), p. 17-28.
503 Hancock, G. S. and Anderson, R. S., 2002. Numerical modeling of fluvial strath-terrace
504 formation in response to oscillating climate. Geological Society of America Bulletin, v.
505 114(9), p. 1131-1142.
506 Heller, P. L. and Paola, C., 1992, The large-scale dynamics of grain-size variation in alluvial
507 basins, 2: Application to syntectonic conglomerate: Basin Research, v. 4, no. 2, p. 91-
508 102.
509 Hjulström, F., 1935, Studies in the morphological activity of rivers as illustrated by the river
510 Fyris: Bulletin of the Geological Institution of the University of Uppsala, v 25, p. 221-
511 528.
512 Hoey, T. B. and Ferguson, R., 1994, Numerical simulation of downstream fining by selective
513 transport in gravel bed rivers: Model development and illustration: Water resources
514 research, v.30, p. 2251-2260.
515 Hovius, N., Stark, C. P. and Allen, P. A., 1997. Sediment flux from a mountain belt derived by
516 landslide mapping. Geology, v. 25(3), p. 231-234.
517 Howard, J.L., 1993. The statistics of counting clasts in rudites: a review with examples from the
518 upper Paleogene of southern California, USA. Sedimentology 40, 157-174.
519 Huffman, G. J., Bolvin, D. T., Nelkin, E. J., Wolff, D. B., Adler, R. F., Gu, G. and Stocker, E. F.,
520 2007, The TRMM multisatellite precipitation analysis (TMPA): Quasi-global, multiyear,
521 combined-sensor precipitation estimates at fine scales. Journal of Hydrometeorology, v.
522 8, no. 1, p. 38-55.
523 Isacks, B. L., 1988. Uplift of the central Andean plateau and bending of the Bolivian orocline.
524 Journal of Geophysical Research: Solid Earth, v. 93(B4), p. 3211-3231.
525 Keefer, D. K., 1984. Landslides caused by earthquakes. Geological Society of America Bulletin,
526 v. 95(4), p. 406-421.
527 Kodoma, Y., 1994, Downstream changes in the lithology and grain size of fluvial gravels, the
528 Watarase River, Japan: Evidence of the role of abrasion in downstream fining: Journal of

529 Sedimentary Research, Section A: Sedimentary Petrology and Processes, v. 64A, p. 68-
530 75.
531 Koiter, A. J., Owens, P. N., Petticrew, E. L. and Lobb, D. A., 2013, The behaviour characteristics
532 of sediment properties and their implications for sediment fingerprinting as an approach
533 for identifying sediment source sin river basins: Earth Science Reviews, v. 125, p. 24-42.
534 Korup, O. and Schlunegger, F., 2009. Rock-type control on erosion-induced uplift, eastern Swiss
535 Alps. Earth and Planetary Science Letters, v. 278(3), p. 278-285.
536 Korup, O. and Weidinger, J. T., 2011. Rock type, precipitation, and the steepness of
537 Himalayan threshold hillslopes. Geological Society, London, Special Publications, v.
538 353(1), p. 235-249.
539 Lisle, T.E., Iseya, F. and Ikeda, H., 1993, Response of a channel with alternate bars to a
540 decrease in supply of mixed-size bed load: A flume experiment: Water resources
541 research, v. 29, p. 3623–3629.
542 Litty, C., Duller, R., and Schlunegger, F., 2016. Paleohydraulic reconstruction of a 40 ka-old
543 terrace sequence implies that water discharge was larger than today. Earth surface
544 processes and landforms.
545 Litty, C., Lanari, P., Burn, M., and Schlunegger, F., 2017, Climate-controlled shifts in sediment
546 provenance inferred from detrital zircon ages, Western Peruvian Andes. Geology. v. 45;
547 no. 1; p. 59–62.
548 Macharé, J., & Ortlieb, L., 1992. Plio-Quaternary vertical motions and the subduction of the
549 Nazca Ridge, central coast of Peru. Tectonophysics, v. 205(1-3), p. 97-108.
550 Marcus, W.A., Ladd, S.C., Stoughton, J.A., Stock, J.W., 1995. Pebble counts and the role of
551 user-dependent bias in documenting sediment size distributions. Water Resources
552 Research, v. 31 (10), p. 2625-2631.
553 Margirier, A., Robert, X., Audin, L., Gautheron, C., Bernet, M., Hall, S., Simon-Labric, T., 2015.
554 Slab flattening, magmatism, and surface uplift in the Cordillera Occidental (northern Peru).
555 Geology, v. 43, p. 1031-1034.
556 McLaren, P. and Bowles, D., 1985, The Effects of Sediment Transport on Grain-Size
557 Distributions: Journal of Sedimentary Petrology, v. 55, p. 457-470.
558 McNulty, B., & Farber, D., 2002. Active detachment faulting above the Peruvian flat slab.
559 Geology, v. 30(6), p. 567-570.

McPhillips, D., Bierman, P. R., & Rood, D. H., 2014. Millennial-scale record of landslides in the Andes consistent with earthquake trigger. Nature Geoscience, v. 7(12), p. 925-930.

Meyer-Peter, E., & Müller, R., 1948. Formulas for bed-load transport. In IAHSR 2nd meeting, Stockholm, appendix 2. IAHR.

Montgomery, D., 2001. Slope distributions, threshold hillslopes, and steady-state topography. American Journal of Science, v. 301, p. 432-454.

Montgomery, D. R., Balco, G. and Willett, S. D., 2001. Climate, tectonics, and the morphology of the Andes. Geology, v. 29(7), p. 579-582.

Mukasa, S. B., 1986. Zircon U-Pb ages of super-units in the Coastal batholith, Peru: Implications for magmatic and tectonic processes. Geological Society of America Bulletin, v. 97(2), p. 241-254.

Nocquet, J. M., Villegas-Lanza, J. C., Chlieh, M., Mothes, P. A., Rolandone, F., Jarrin, P. and Martin, X., 2014. Motion of continental slivers and creeping subduction in the northern Andes. Nature Geoscience, v. 7(4), p. 287-291.

Noury, M., Bernet, M., Schildgen, T. F., Simon-Labric, T., Philippon, M., & Sempere, T., 2016. Crustal-scale block tilting during Andean trench-parallel extension: Structural and geo-thermochronological insights. Tectonics, v. 35(9), p. 2052-2069.

Ouimet, W. B., Whipple, K. X., & Granger, D. E., 2009. Beyond threshold hillslopes: Channel adjustment to base-level fall in tectonically active mountain ranges. Geology, v. 37(7), p. 579-582.

Paola, C., Heller, P. L. and Angevinet, C. L., 1992a, The large-scale dynamics of grain-size variation in alluvial basins, 1: Theory: Basin Research, v. 4, p. 73-90.

Paola, C. and Seal, R., 1995, Grain size patchiness as a cause of selective deposition and downstream fining: Water Resources Research, v. 31, p. 1395-1407.

Parker, G., 1991, Selective sorting and abrasion of river gravel. 1: Theory: Journal of Hydraulic Engineering, v. 117, no. 2, p. 131-147.

Parker, R. N., Densmore, A. L., Rosser, N. J., De Michele, M., Li, Y., Huang, R. & Petley, D. N., 2011. Mass wasting triggered by the 2008 Wenchuan earthquake is greater than orogenic growth. nature geoscience, v. 4(7), p. 449-452.

Pearson, K., 1895, Notes on regression and inheritance in the case of two parents, Proceedings of the Royal Society of London, v. 58, p. 240–242.

591 Ramos, V. A., 2010. The tectonic regime along the Andes: Present-day and Mesozoic regimes.
592 Geological Journal, v. 45(1), p. 2-25.
593 Rasband, W.S., ImageJ, U. S. National Institutes of Health, Bethesda, Maryland, USA,
594 http://imagej.nih.gov/ij/, 1997-2016.
595 Reber, R., Delunel, R., Schlunegger, F., Litty, C., Madella, A., Akçar, N., Christl, M.
596 Environmental controls on 10Be-based catchment averaged denudation rates along the
597 western margin of the Peruvian Andes. Terra Nova.
598 Regard, V., Saillard, M., Martinod, J., Audin, L., Carretier, S., Pedoja, K. and Hérail, G., 2010.
599 Renewed uplift of the Central Andes Forearc revealed by coastal evolution during the
600 Quaternary. Earth and Planetary Science Letters, v. 297(1), p. 199-210.
601 Reuter, H. I., Nelson, A. and Jarvis, A., 2007. An evaluation of void-filling interpolation
602 methods for SRTM data. International Journal of Geographical Information Science, v.
603 21(9), p. 983-1008.
604 Rice, S. and Church, M., 1998, Grain size along two gravel-bed rivers: Statistical variation,
605 spatial pattern and sedimentary links: Earth Surface Processes and Landforms, v. 23, p.
606 345-363.
607 Robinson, R. A. and Slingerland, R. L., 1998, Origin of fluvial grain-size trends in a foreland
608 basin: the Pocono Formation on the central Appalachian basin: Journal of Sedimentary
609 Research, v. 68, no. 3.
610 Schildgen, T. F., Hodges, K. V., Whipple, K. X., Reiners, P. W. and Pringle, M. S., 2007, Uplift
611 of the western margin of the Andean plateau revealed from canyon incision history,
612 southern Peru. Geology 35, 523–526.
613 Schlunegger, F., Norton, K.P., Caduff, R., 2013. Hillslope processes in temperate environments.
614 In: John F. Shorder (ed.): Treatise on Geomorphology, v. 7: p. 337-345, San Diego:
615 Academic Press.
616 Schumm, S. A. and Stevens, M. A., 1973, Abrasion in place: a mechanism for rounding and size
617 reduction of coarse sediments in rivers: Geology, v. 1, p. 37-40.
618 Sébrier, M., Mercier, J. L., Macharé, J., Bonnot, D., Cabrera, J., & Blanc, J. L., 1988. The state
619 of stress in an overriding plate situated above a flat slab: The Andes of central Peru.
620 Tectonics, v. 7(4), p. 895-928.

621 Shields, A., 1936, Anwendung der Ahnlichkeitsmekanik und der Turbulenzforschung auf die
622 Geschiebebewegung, Mittelung der preussischen Versuchsanstalt für Wasserbau und
623 Schiffbau, 26. (Berlin).
624 Sneed, E.D., and Folk, R.L., 1958. Pebbles in the lower Colorado River, Texas a study in particle
625 morphogenesis. The Journal of Geology, 114-150.
626 SNIRH; Sistema Nacional de Informacion de Recursos Hidricos. http://snirh.ana.gob.
627 pe/consultasSnirh/ConsHidrom2.aspx
628 Steffen, D., Schlunegger, F., and Preusser, F., 2010, Late Pleistocene fans and terraces in the
629 Majes valley, southern Peru, and their relation to climatic variations. International
630 Journal of Earth Sciences, v. 99(8), p. 1975-1989.
631 Sternberg, H., 1875, Untersuchungen über längen-und Querprofil geschiebeführender Flüsse, Z.
632 Bauwes., 25, 486–506.
633 Surian, N., 2002, Downstream variation in grain size along an Alpine river: analysis of
634 controls and processes: Geomorphology, v. 43, p. 137-149.
635 Trauerstein, M., Norton, K. P., Preusser, F., and Schlunegger, F., 2013, Climatic imprint on
636 landscape morphology in the western escarpment of the Andes. Geomorphology, v. 194,
637 p. 76-83.
638 Vidal, J. C., 1993, Geologia de los cuadrangulos de Huambo y Orcopampa, v 46. Instituto
639 Geologico Minero y Metalurgico, Lima.
640 Whittaker, A. C., Cowie, P. A., Attal, M., Tucker, G. E. and Roberts, G. P., 2007, Bedrock
641 channel adjustment to tectonic forcing: Implications for predicting river incision rates:
642 Geology, v. 35, no. 2, p.103-106.
643 Whittaker, A. C., Attal, M. and Allen, P.A., 2010, Characterising the origin, nature and fate of
644 sediment exported from catchment perturbed by active tectonics. Basin Research. v. 22. p.
645 809-828.
646 Wittmann, H., von Blanckenburg, F., Kruesmann, T., Norton, K. P., and Kubik, P. W., 2007.
647 Relation between rock uplift and denudation from cosmogenic nuclides in river sediment
648 in the Central Alps of Switzerland. Journal of Geophysical Research: Earth Surface,
649 112(F4).
650
651 **FIGURES AND TABLES CAPTIONS**

652

653 **Table 1:** Location of the sampling sites with the altitude in meters above sea level. The table also
654 displays grain size results together with the rivers' and basins' properties and hydrological
655 properties.

656

657 **Table 2:** Location of the sampling sites in the Majes basin and grain size results in the Majes
658 basin.

659

660 **Table 3:** Results of the statistical investigations, illustrated here as correlation matrix of the r-
661 values. The valuess in bold show significant correlation between the grain size data and the
662 different catchment scale properties.

663

664

665 **Figure 1: A:** Map of the studied basins showing the sampling sites and the western escarpment
666 (western escarpment modified after Trauerstein et al., 2013). The purple strip east of the trench
667 axis corresponds to the swath over which the historical earthquake data, presented in Figure 3,
668 The map also illustrates the location of the buoyant Nazca ridge, depth of the slab in dashed line,
669 plus patterns of earthquake occurrence. **B:** Geological map of the western Peruvian Andes. **C:**
670 Map of the precipitation rates showing the spatial extent of the ITCZ, modified after Huffman et
671 al., 2007.

672

673

Figure 2: Topography of subducting Nazca plate, where slab depth data has been extracted from earthquake.usgs.gov/data/slab/ modified form Reber et al., 2017. This N-S projection also illustrates: a) tectonic lineaments such as submarine ridges and MFZ: Mendaña Fracture Zone; NFZ: Nazca Fracture Zone; b) Holocene Volcanoes; c) Earthquake data, taken from earthquake.usgs.gov/earthquakes/search/; number of earthquakes M>4 within 30 km radius window. d) Coastal elevation. The data has been extracted from a 20 km-wide swath prole along the coast. The three lines represent maximum, mean and minimum elevations within the selected swath; e) Catchment averaged denudation rates have been corrected for quartz contents (Reber et al. 2017); f) Mean annual precipitation rates (Reber et al., 2017); g) Mean annual water discharge (Reber et al., 2017); h) Grain size results for the intermediate (b)-axis of the pebbles in the rivers from north to south at the sampling sites presented in Figure 1; i) Ratio between the intermediate axis and the long (a)-axis (modied after Reber et al., 2017). Exceptionally larger D_{50} values of 4-6 cm were measured for basins situated between 11-12°S and 16-17°S where hillslope gradients are steeper than 0.4 on the average (i.e., 20-22°), or where mean annual stream flows exceed the average values of the western Peruvian streams (10-40 m^3/s) by a factor of 2.

Figure 3: Geological map of the Majes basin overlain by the precipitation pattern (Precipitation data from Steffen et al., 2010), where the black dashed lines show precipitation rates (mm/yr). GS1 to GS5 represent sites where grain size data has been collected. The right corner shows the Majes river long profile.

Figure 4: Grain size results along the Majes River.

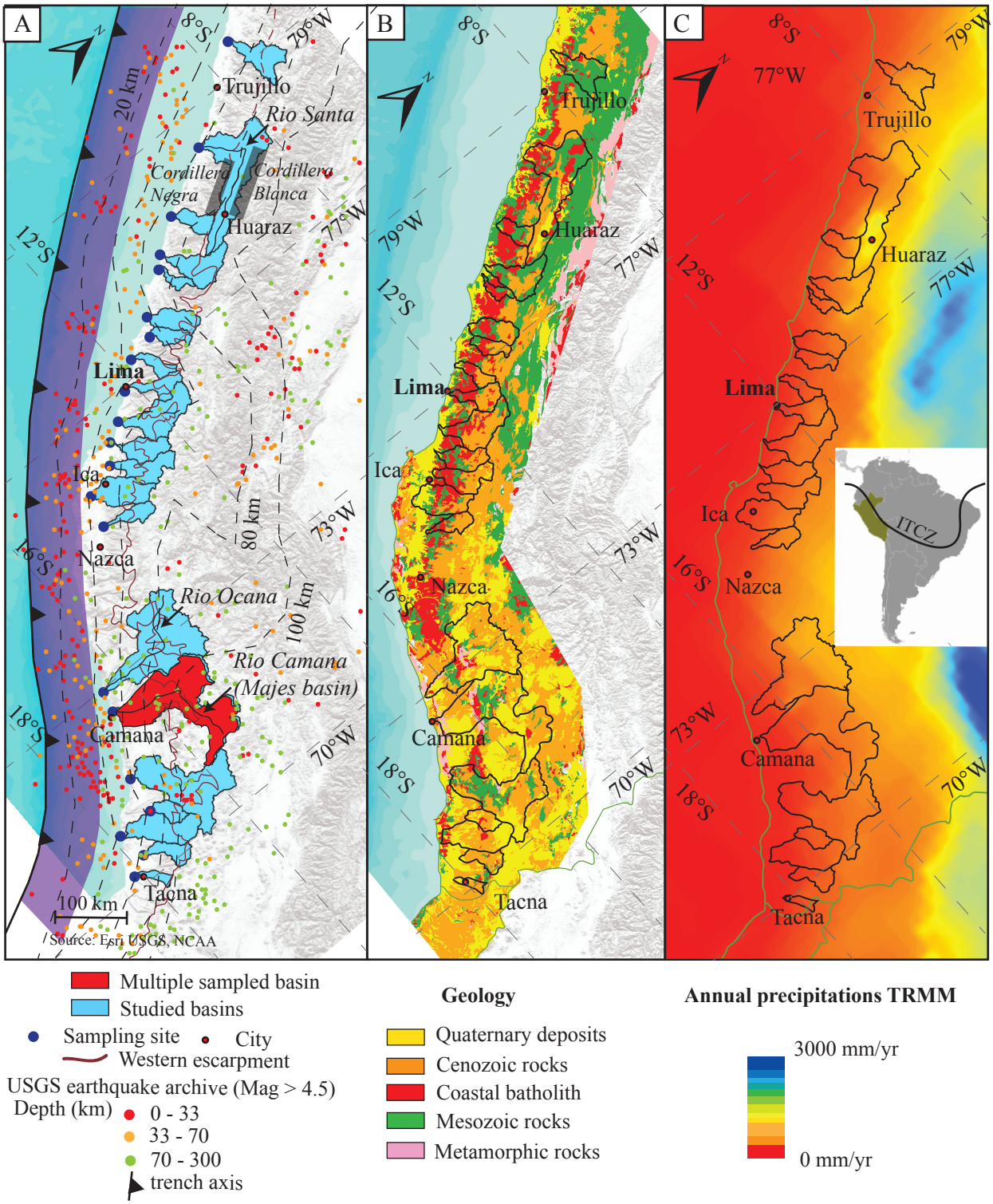
A
B
C
8°S
79°W
77°W
12°S
16°S
18°S
73°W
70°W
Trujillo
Rio Santa
Cordillera Negra
Cordillera Blanca
Huaraz
Lima
Ica
Nazca
Rio Ocana
Rio Camana (Majes basin)
Camana
Tacna
20 km
80 km
100 km
100 km
Source: Esri, USGS, NCAA
ITCZ
Multiple sampled basin
Studied basins
Sampling site
City
Western escarpment
USGS earthquake archive (Mag > 4.5)
Depth (km)
0 - 33
33 - 70
70 - 300
trench axis
Geology
Quaternary deposits
Cenozoic rocks
Coastal batholith
Mesozoic rocks
Metamorphic rocks
Annual precipitations TRMM
3000 mm/yr
0 mm/yr

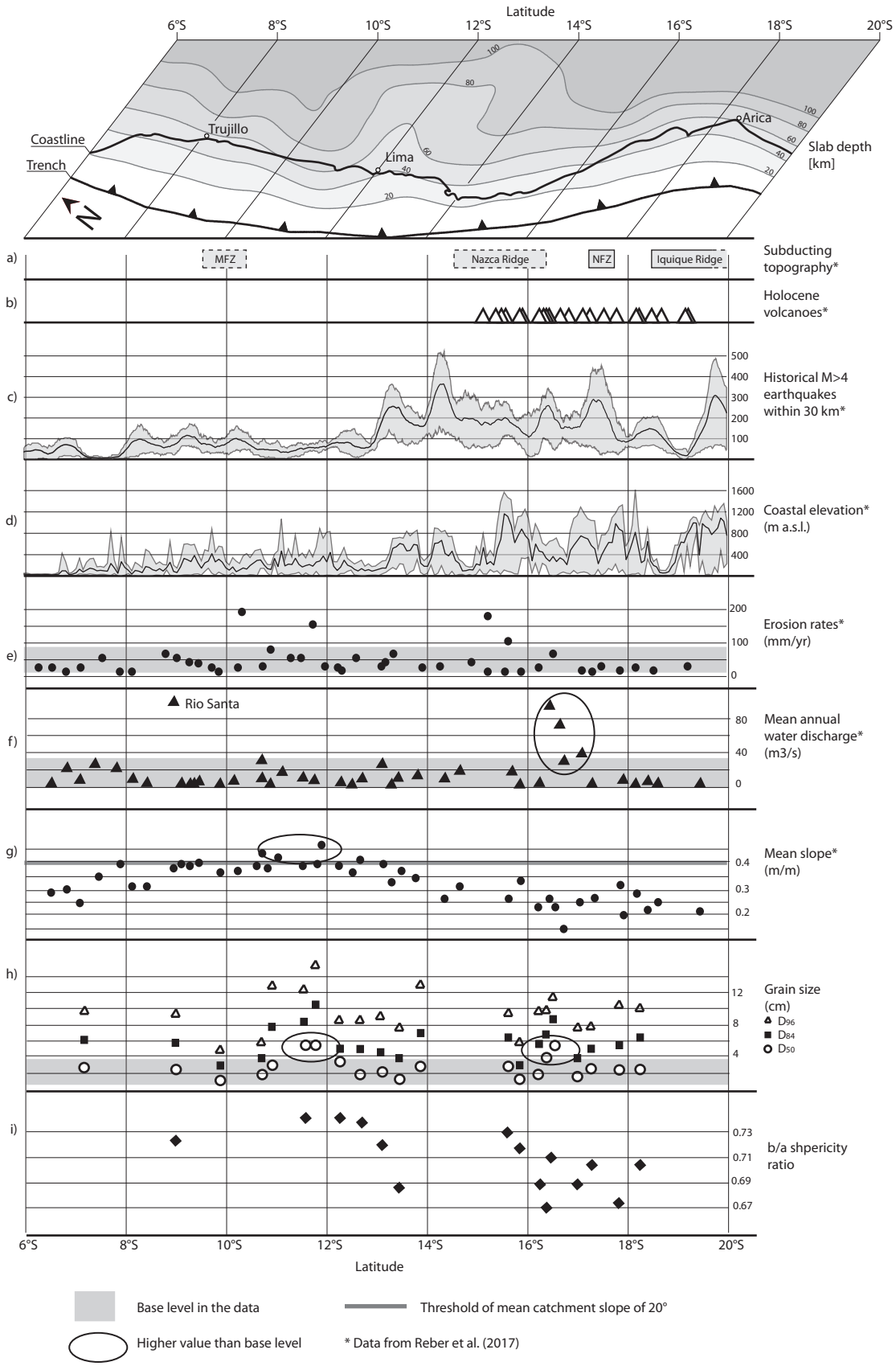
Latitude
6°S
8°S
10°S
12°S
14°S
16°S
18°S
20°S
Coastline
Trench
Trujillo
Lima
Arica
Slab depth [km]
a)
MFZ
Nazca Ridge
NFZ
Iquique Ridge
Subducting topography*
b)
Holocene volcanoes*
c)
Historical M>4 earthquakes within 30 km*
d)
Coastal elevation* (m a.s.l.)
e)
Erosion rates* (mm/yr)
f)
Rio Santa
Mean annual water discharge* (m3/s)
g)
Mean slope* (m/m)
h)
Grain size (cm)
D96
D84
D50
i)
b/a shpericity ratio
Base level in the data
Threshold of mean catchment slope of 20°
Higher value than base level
* Data from Reber et al. (2017)

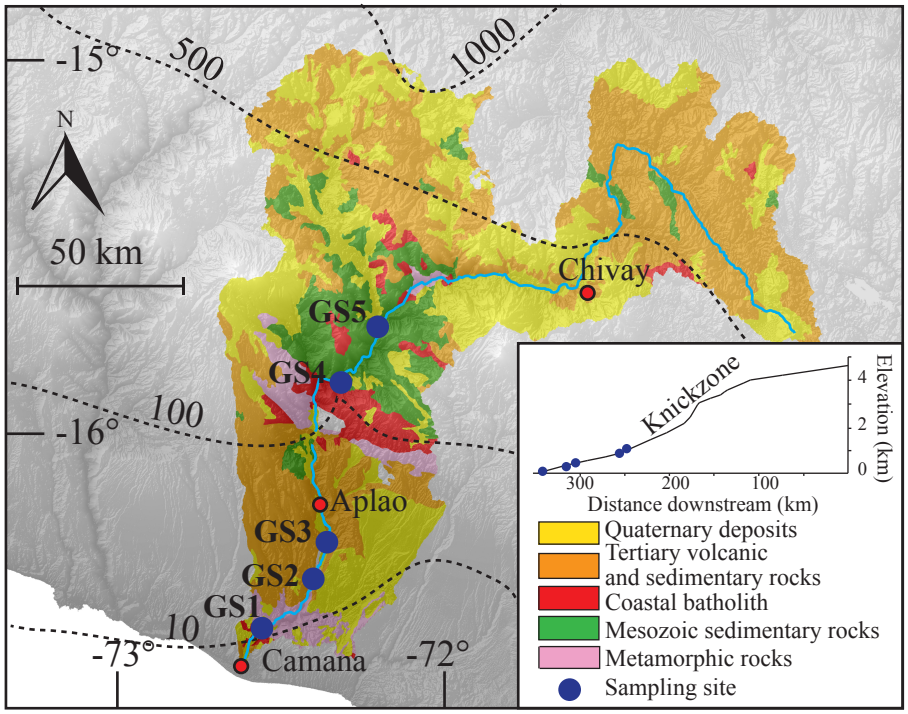
-15°
500
1000
N
50 km
Chivay
GS5
GS4
100
-16°
Aplao
GS3
GS2
GS1
10
-73°
Camana
-72°
Knickzone
Elevation (km)
4
2
0
300
200
100
Distance downstream (km)
Quaternary deposits
Tertiary volcanic
and sedimentary rocks
Coastal batholith
Mesozoic sedimentary rocks
Metamorphic rocks
Sampling site

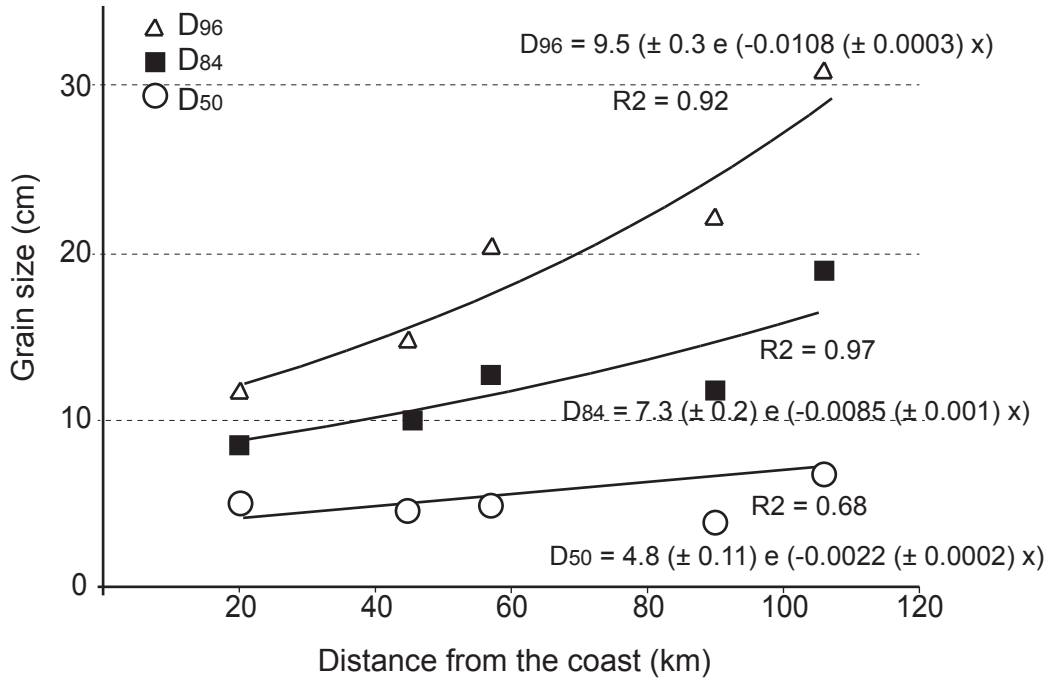

Figure 4: Grain size results along the Majes River.

River name	Sample name	Altitude (m)	Latitude (DD WGS84)	Longitude (DD WGS84)	D50 (cm)	D84 (cm)	D96 (cm)	b/a	Catchment area (km2)	Mean basin slope (m/m) (Reber et al., 2017)	Slope at the sampling site (m/m)	Distance form the western escarpment (km)	Channel width at the sampling site (m)	Mean annual water discharge (m3/s) (Reber et al., 2017)	Shear stress (kg/m.s2)	Sediment flux (m3/s)	Denudation rates (mm/ka) (Reber et al., 2017)	Denudation rates uncertainties (mm/ka) (Reber et al., 2017)	Denudation rates corrected for Qz content in bedrock (mm/ka) (Reber et al., 2017)
Tacna	PRC-ME1	231	-18.12	-70.33	2.3	6.2	10.0	0.70	899	0.28	0.015	48	6	3.4	142.68	11952	13.3	3.6	12.2
Rio Sama Grande	PRC-ME3	455	-17.82	-70.51	2.5	5.5	10.6	0.67	2150	0.3	0.013	73	6	4	114.14	61495	28.6	5.3	27.7
Ilo / Rio Osmore	PRC-ME5	1072	-17.29	-70.99	2.6	5.1	7.8	0.70	1783	0.26	0.018	53	7	3.4	184.18	38146	21.4	4.8	18.6
Rio Tambo	PRC-ME6	145	-17.03	-71.69	1.5	3.6	7.5	0.69	12885	0.24	0.051	141	26	38.1	265.69	1155744	89.7	16.7	72.1
Tambillo / Rio Sihuas	PRC-ME802	117	-16.34	-72.13	2.0	6.0	10.0	0.69	1708	0.15	0.019	70	15	30.1	88.78	58087	34	6.4	27.7
Camana / Rio Majes	PRC-ME7	69	-16.51	-72.64	5.2	8.7	11.6	0.67	17401	0.23	0.005	188	100	68.4	46.06	2218568	127.5	23.4	106.8
Ocona / Rio Ocona	PRC-ME9	14	-16.42	-73.12	4.8	6.8	10.0	0.71	16084	0.26	0.004	192	70	91.1	26.25	3893878	242.1	45	184.1
Nasca / Rio Grande	PRC-ME1402	15	-15.85	-74.26	1.3	3.0	6.0	0.71	1412	0.32	0.014	48	3	20.4	34.10	65093	46.1	8.6	29.4
Chacaltana / Rio Ica	PRC-ME15	3	-15.63	-74.64	2.9	6.4	9.6	0.73	4677	0.26	0.003	88	23	12.1	33.01	126266	27	5.7	25.1
Humay District / Rio Pisco	PRC-ME16	400	-13.73	-75.89	3	6.6	13		3649	0.34	0.013	62	20	13.6	112.91	379865	104.1	20.4	69.1
Chinca Alta / Rio San Juan	PRC-ME17	75	-13.47	-76.14	1.3	3.8	7.6	0.69	3090	0.37	0.01	78	5	10.1	48.54	189112	61.2	11.7	44.1
Rio Canete	PRC-ME19	23	-13.12	-76.39	2	4.6	8.8	0.72	6029	0.4	0.01	100	60	26.4	112.24	402743	66.8	12.3	51.2
Rio Omas	PRC-ME20	33	-12.67	-76.65	1.6	4.8	8.8	0.73	2322	0.41	0.0076	78	22	8.2	95.14	62913	27.1	5.4	17.9
Rio Lurin	PRC-ME22	40	-12.25	-76.89	3	5	8.8	0.74	1572	0.38	0.022	70	5	3.7	176.26	60515	38.5	7.1	23.6
Lima / Rio Chillon	PRC-ME39	402	-11.79	-76.99	5.3	10.5	15.5		1755	0.39	0.018	51	40	4.9	392.89	144272	82.2	15.5	53.4
Rio Chancay	PRC-ME23	72	-11.61	-77.24	5.5	8.3	12.5	0.74	3059	0.39	0.01	66	20	8.9	111.55	298866	97.7	18.4	52.8
Rio Supe	PRC-ME25	74	-11.07	-77.59	2.8	7.7	13		4306	0.38	0.012	82	5	3.8	98.55	179550	41.7	7.7	25.6
Rio Pativilca	PAT-ME	10	-10.72	-77.77	1.8	3.6	6		4607	0.44	0.014	74	30	30.9	96.30	1198281	260.1	48.8	190.9
Huarmey	PRC-ME38	24	-10.07	-78.16	1.7	3.4	5.2		2072	0.37	0.004	78	15	9.8	38.34	40816	19.7	4.5	10.1
Rio Santa	PRC-ME27	80	-8.97	-78.62	2	5.4	9	0.72	12313	0.38	0.005	65	40	96.1	23.08	876699	71.2	13.4	70.4
San Martin de Porres	PRC-ME30	67	-7.32	-79.48	2.9	6.3	10		3882	0.34	0.007	126	40	25.4	65.72	118401	30.5	5.9	25.8

Table 1 : Location of the sampling sites with the altitude in meters above sea level.
The table also displays grain size results together with the rivers' and basins' properties and hydrological properties.
Morphometric dataset for the sampled drainage basins. All calculations are based on the 90 m resolution DEM (NASA)
The precipitation, water discharge data and the denudation rates are from Reber et al., in review

	Distance from the coast (km)	Altitude (m)	Latitude (°)	Longitude (°)	D50	D84	D96	b/a
GS1	20	69	-16.51	-72.64	5.2	8.7	11.6	0.67
GS2	45	283	-16.37	-72.49	4.8	10	15	0.69
GS3	57	378	-16.28	-72.45	5.4	12.7	21	0.65
GS4	90	700	-16.00	-72.48	3.3	12	22.5	0.67
GS5	106	882	-15.86	-72.45	6.2	19	31	0.71

Table 2: Location of the sampling sites in the Majes basin and grain size results in the Majes basin.

	Altitude (m)	*Latitude (DD WGS84)*	*Longitude (DD WGS84)*	***D50 (cm)***	***D84 (cm)***	***D96 (cm)***	***b/a***	*Catchment area (km2)*	*Mean slope (m/m)*	*Distance form the western escarpment (km)*	*Mean annual water discharge (m3/s)*	*Shear stress (kg/m.s2)*	*Sediment flux (m3/s)*	*Denudation rates (mm/ka)*	*Denudation rates corrected for Qz content in bedrock (mm/ka)*
Altitude (m)	1.00														
Latitude (DD WGS84)	-0.36	1.00													
Longitude (DD WGS84)	0.46	-0.97	1.00												
D50 (cm)	0.09	0.00	-0.01	1.00											
D84 (cm)	0.14	0.04	-0.03	0.87	1.00										
D96 (cm)	0.18	0.02	-0.02	0.73	0.93	1.00									
b/a	-0.30	0.66	-0.71	0.09	0.00	-0.02	1.00								
Catchment area (km2)	-0.25	-0.12	0.12	0.31	0.16	0.04	-0.25	1.00							
Mean slope (m/m)	-0.23	0.72	-0.78	-0.07	-0.10	-0.03	0.63	-0.28	1.00						
Distance form the western escarpment (km)	-0.32	-0.14	0.14	0.35	0.16	0.03	-0.33	0.84	-0.35	1.00					
Mean annual water discharge (m3/s) (Reber et al., 2017)	-0.30	0.03	-0.01	0.18	0.05	-0.07	-0.13	0.87	-0.23	0.64	1.00				
Shear stress (kg/m.s2)	0.45	-0.11	0.14	0.23	0.33	0.39	-0.06	-0.21	0.06	-0.23	-0.37	1.00			
Sediment flux (m3/s)	-0.23	-0.19	0.17	0.42	0.17	0.03	-0.21	0.86	-0.24	0.82	0.80	-0.22	1.00		
Denudation rates (mm/ka) (Reber et al., 2017)	-0.23	0.04	-0.09	0.34	0.09	0.00	-0.09	0.56	0.12	0.48	0.56	-0.07	0.79	1.00	
Denudation rates corrected for Qz content in bedrock (mm/ka) (Reber et al., 2017)	-0.22	0.01	-0.04	0.30	0.06	-0.03	-0.17	0.64	0.05	0.54	0.65	-0.11	0.84	0.99	1.00

Table 3: Results of the statistical investigations, illustrated here as correlation matrix values.